Dalton Transactions

Accepted Manuscript

ROYAL SOCIETY OF CHEMISTRY

www.rsc.org/dalton

1D-3D Mixed-Ligand Frameworks with an Unusual *dmp* Topology Tuned by Intersection Angles of Isomeric Benzenedicarboxylates: Magnetic Properties, Gas-Dependent Calcination-thermolysis and Energy Storage Performances

Zuo-Xi Li,[*[a, b]] Gan Ye,[[a]] Juan Han,[[a]] Ying Yang,[[a]] Kang-Yu Zou,[[a]] Xin Wang,[[a]] Xiao-Ling Wang[[b]] and Xiao-Feng Gou[[a]]

[a]*Key Laboratory of Synthetic and Natural Functional Molecule Chemistry (Ministry of Education), Shaanxi Key Laboratory of Physico-Inorganic Chemistry, College of Chemistry and Material Sciences, Northwest University, Xi'an 710069, P.R.China;*

[b]*Shannxi Key Laboratory of Phytochemistry, Baoji 721016, P.R.China.*

*Corresponding author. E-mail: Lizx@nwu.edu.cn

***To Dalton Transactions* (Article)**

ABSTRACT

In this work, three isomeric benzenedicarboxylates, 1,2-benzenedicarboxylic acid (*o*-H_2**bdc**), 1,3-benzenedicarboxylic acid (*m*-H_2**bdc**), and 1,4-benzenedicarboxylic acid (*p*-H_2**bdc**), have been utilized as the ancillary ligands to perform a systematic study on the structure diversity of mixed-ligand frameworks. The solvothermal reactions of $Co(NO_3)_2$ with these aromatic acids and the primary ligand 4,4'-bis(imidazolyl)biphenyl (**bibp**) afford three novel coordination polymers, $\{[Co_6(\mathbf{bibp})_3(o\text{-}\mathbf{bdc})_6(H_2O)](CH_3CN)_{1.5}\}_\infty$ (**1**), $[Co(\mathbf{bibp})(m\text{-}\mathbf{bdc})]_\infty$ (**2**), and $[Co(\mathbf{bibp})(p\text{-}\mathbf{bdc})]_\infty$ (**3**). Owing to different orientations of carboxylate groups, the benzenedicarboxylates adopt various bridging modes to connect Co^{II} ions into a series of 1D carboxylate∩cobalt architectures based on the 1D chain, binuclear and single-ion magnetic units, respectively. These 1D architectures are further decorated by the **bibp** ligand to afford a 1D belt for **1**, 2D double-bridging (4,4) sheet for **2**, and 3D unusual ***dmp*** framework for **3**. Significantly in **3**, three equivalent frameworks are interlocked with each other to represent an unprecedented three-fold interpenetrating ***dmp*** network. The structural diversity indicates that the benzenedicarboxylate plays an essential role in the assembly of mixed-ligand frameworks, and the orientation of carboxylate group exerts an important influence on the nucleation, dimensionality and also interpenetration. Furthermore, magnetic properties of **1** and **2** have been studied by fitting the experimental data as possible, and the magneto-structural correlation of **2** has been also well discussed. Importantly, CoO and Co_3O_4 were obtained from the controllable thermolysis of crystals of **1** via the simple calcination treatment under different gas environments. The as-synthesized cobalt oxides display good crystalline and appear as micro- or nanoparticles, which can be applied as supercapacitor electrodes through the energy storage performance in 2 M KOH electrolyte.

Introduction

Coordination polymers (CPs) are assembled from the metal ion (or cluster) and organic ligand, where the ligand acts as the "strut" bridging the metal unit ('joint') in turn to afford a multi-dimensional completely ordered architecture.[1] The intriguing topological feature as well as the potential candidate for the functional material makes the design and synthesis of CPs attract a great deal of attention.[2] Since the physico-chemical property is extremely dependant on the crystal structure, it is very important to control over the topology framework and rationally construct CPs with predicted structures. According to the definition of CPs, the topological structure seems most related to the ligand backbone, and the effect of organic ligand is an indispensable and everlasting research topic.[3]

The rapid development of CPs has been experiencing great success in creating a number of molecular magnets, which exhibit slow magnetic relaxation and quantum tunneling.[4] Another major target in molecular magnetism is the construction of novel magnetic unit, and then the exploration of magneto-structural correlation by theoretical simulation of magnetic coupling.[5] However, it is still a challenging scientific endeavor to quantitatively analyze the strength of magnetic exchange interaction, partly owing to the lack of reliable strict models for some complicated systems. On the other hand, the large uniaxial magnetic anisotropy, for example, in the octahedral Co^{II} ion, leads to significant spin-orbital coupling effect and unquenched orbital angular momentum, undoubtedly making the magnetic fitting even more difficult.[6] Excitedly, the enhanced magnetic anisotropy could increase the blocking temperature T_b according the equation $U = S_T^2|D|$ or $(S_T^2 - 1/4)|D|$.[7] Thus the Co^{II} system with large anisotropic feature is very interesting.

CPs have emerged as a class of functional materials with highly ordered architectures, large specific surface and regular shapes. Solid-state thermolysis of CPs as precursors may provide a very promising opportunity to generate metal oxide nanomaterials with ultrahigh porosity.[8] The calcination strategy is simple, inexpensive, controllable and scalable. Despite the progress achieved to date, research on the facile synthesis of nanostructure inorganic materials derived from CPs is still in its early stage.[9] Thus it is highly desirable to develop novel synthesis protocols and concepts utilizing CPs to prepare high-quality functional nanomaterials with unique morphologies.

In this paper, 4,4′-bis(imidazol-1-yl)-biphenyl **(bibp)** is chosen as the primary ligand, where a series of benzenedicarboxylates, 1,2-benzenedicarboxylic acid (*o*-H_2**bdc**), 1,3-benzenedicarboxylic acid (*m*-H_2**bdc**), and 1,4-benzenedicarboxylic acid (*p*-H_2**bdc**), are utilized as ancillary ligands to react with $Co(NO_3)_2$ under

the solvothermal environment. Finally, three novel CPs with mixed-ligand frameworks, $\{[Co_6(\mathbf{bibp})_3(o\text{-}\mathbf{bdc})_6(H_2O)](CH_3CN)_{1.5}\}_\infty$ (**1**), $[Co(\mathbf{bibp})(m\text{-}\mathbf{bdc})]_\infty$ (**2**) and $[Co(\mathbf{bibp})(p\text{-}\mathbf{bdc})]_\infty$ (**3**), have been obtained and characterized. The relationship between the topological structure and benzoate backbone was discussed, and magnetic properties of **1** and **2** have been well investigated. Significantly, CoO and Co_3O_4 particles were obtained from the gas-controllable calcination-thermolysis of crystals of **1**, which have been employed as electrode materials for supercapacitors.

Experimental Section

Materials and General Methods. All the solvents and reagents were commercially available and used as received. The ligand **bibp** was synthesized according to the reported procedure.[10] Elemental analyses of C, H, and N were performed on a Perkin-Elmer 240C analyzer. IR spectra were measured on a TENSOR 27 (Bruker) FT-IR spectrometer with KBr pellets. The thermogravimetry (TG) experiment was carried out on a Rigaku standard TG analyzer under N_2 atmosphere with a heating rate of 10 °C·min^{-1} in the temperature range of 15-600 °C. The powder X-ray diffraction (XRD) was recorded on a Rigaku D/Max-2500 diffractometer at 40 kV, 100 mA for a Cu-target tube and a graphite monochromater. Magnetic data were collected on a Quantum Design MPMS-XL SQUID magnetometer equipped with a 5T magnet using the crushed crystal sample. The diamagnetic corrections were calculated using Pascal's constants. The morphologies and structures of CoO and Co_3O_4 samples were observed by scanning electron microscopy (SEM, SHIMADZU, SSX-550) and field emission scanning electron microscopy (FE-SEM, JEOL, JSM-6700F), respectively.

Syntheses of CPs 1-3.

Single crystals of **1-3** suitable for X-ray analysis were all obtained by the solvothermal method.

$\{[Co_6(bibp)_3(o\text{-}bdc)_6(H_2O)](CH_3CN)_{1.5}\}_\infty$ (1). The suspension of $Co(NO_3)_2{\cdot}6H_2O$ (0.2 mmol, 58 mg), **bibp** (0.1 mmol, 29 mg) and *o*-H_2**bdc** (0.2 mmol, 33 mg) in 14 mL component solvent (CH_3CN:H_2O = 4:3) was sealed in a Teflon-lined autoclave and heated to 125 °C for 3 days. After the autoclave was cooled to room temperature at 5 °C·h^{-1}, purple needle crystals with suitable diameters for single crystal X-ray crystallographic analysis were obtained. The mother liquor was decanted, and crystals were rinsed three times with acetonitrile (8 mL × 3) and dried in air for 4 h. yield: ~70% (hand-picking crystals, based on **bibp**). Anal. Calcd. for $C_{105}H_{72.5}Co_6N_{13.5}O_{25}$: C, 55.39; H, 3.21; N, 8.30%. Found: C, 55.15; H, 3.28; N. 8.41%. IR (KBr, cm^{-1}): 3553w, 3413s, 3123s, 2361m, 1556s, 1520s, 1393s, 1310s, 1262m, 1126m, 1066s, 963m, 818s, 754s, 652m, 462w (Figure **S1-a**).

[Co(bibp)(*m*-bdc)]$_\infty$ (2). A mixture of $Co(NO_3)_2 \cdot 6H_2O$ (0.2 mmol, 58 mg), **bibp** (0.1 mmol, 29 mg) and *m*-H_2**bdc** (0.2 mmol, 33 mg) was suspended in 14 mL component solvent (C_2H_5OH:H_2O = 4:3). After addition of 0.1 mL ammonia water, the suspension was heated in a Teflon-lined autoclave (25 mL) at 185 °C for 3 days. After the autoclave was cooled to room temperature at 5 °C·h^{-1}, pink block crystals with a small amount of powder were obtained. The mother liquor was decanted, and crystals were rinsed three times with ethanol (8 mL × 3) and dried in air for 4 h. yield: ~20% (hand-picking crystals, based on **bibp**). Anal. Calcd. for $C_{26}H_{18}CoN_4O_4$: C, 61.31; H, 3.56; N, 11.00%. Found: C, 61.04; H, 3.62; N. 11.14%. IR (KBr, cm^{-1}): 3706m, 3412w, 3107s, 3067s, 2361s,1624s, 1602s, 1580s, 1515s, 1453s, 1391s, 1242s, 1125m, 1062m, 979w, 961w, 915m, 755s, 720s, 523w, 414w (Figure **S1-b**).

[Co(bibp)(*p*-bdc)]$_\infty$ (3). The suspension of $Co(NO_3)_2 \cdot 6H_2O$ (0.2 mmol, 58 mg), **bibp** (0.1 mmol, 29 mg) and *p*-H_2**bdc** (0.2 mmol, 33 mg) in 14 mL component solvent (C_2H_5OH:H_2O = 4:3) was sealed in a Teflon-lined autoclave and heated to 165 °C for 3 days. After the autoclave was cooled to room temperature at 5 °C·h^{-1}, purple spindle crystals with quite an amount of powder were obtained. The mother liquor was decanted, and crystals were rinsed three times with ethanol (8 mL × 3) and dried in air for 4 h. yield: ~15% (hand-picking crystals, based on **bibp**). Anal. Calcd. for $C_{26}H_{18}CoN_4O_4$: C, 61.31; H, 3.56; N, 11.00%. Found: C, 61.05; H, 3.61; N. 11.13%. IR (KBr, cm^{-1}): 3691m, 3412w, 3129s, 2361s, 2340s, 1630m, 1593s, 1515s, 1390s, 1309s, 1239s, 1125s, 1007m, 961m, 829s, 755s, 654w, 559m, 524w. (Figure **S1-c**).

Syntheses of CoO and Co_3O_4 Particles.

During the synthesis of **1**, the product appears as high-yield needle crystals with lengths of about 0.5 cm in the maximum. Thus **1** is easy to be collected in abundance, and suitable as a precursor to prepare cobalt oxides through the calcination treatment.

For the preparation of CoO particles, the as-synthesized crystals were placed in a tube furnace and heated under N_2 gas flow at 400 °C for 3 h with a heating rate of 10 °C·h^{-1}. Then the tube furnace was naturally cooled to room temperature. Black powder was obtained, which was placed in a furnace at 900 °C for 1 h in the air with a heating rate of 5 °C·min^{-1} to remove the carbon residue. After cooled under N_2 gas, gray CoO particles were gained. XRD peaks (2θ): 36.662, 42.571, 61.643, 73.798, and 77.652°.

For the Co_3O_4 particles, the as-synthesized crystals were placed in a furnace and heated at 400 °C for 3 h with a heating rate of 10 °C·h^{-1} when both ends opening to the air. Then the furnace was naturally cooled to room temperature, and black Co_3O_4 powder was obtained. XRD peaks (2θ): 19.091, 31.365, 36.938, 38.697,

44.883, 55.497, 59.469, and 65.280°.

X-ray Data Collection and Structure Determinations. X-ray single-crystal diffraction data of **1-3** were collected on a Rigaku MM-007/Saturn 70 with graphite monochromatic Mo-Kα radiation (λ = 0.71073 Å). The program SAINT[11] was used for integration of the diffraction profiles. All the structures were solved by direct methods using the SHELXS program of the SHELXTL package and refined by full-matrix least-squares methods with SHELXL.[12] Metal atoms in each complex were located from the *E*-maps and other non-hydrogen atoms excluded in counterions were located in successive difference Fourier syntheses and refined with anisotropic thermal parameters on F^2. The hydrogen atoms of organic ligands were generated theoretically onto the specific atoms and refined isotropically. However, hydrogen atoms of water molecules in **1** could not be theoretically generated, and they also have not been added by difference Fourier maps due to the lack of large enough Q peaks around the water oxygen atom. The free acetonitrile molecule in **1** is highly disordered, and the contribution of solvent electron density was removed by the SQUEEZE routine in PLATON.[13] Further details for structural analysis are summarized in Table **1**, and selected bond lengths and angles for **1-3** are listed in Table **S1**.

(Insert Table **1**)

Electrochemical Performance Measurements. All electrochemical measurements were performed using a CHI660D potentiostat (Chenhua Instrument Co. Ltd., Shanghai, China) coupled with a three-electrode system at room temperature. CoO and Co_3O_4 particles were coated in a nickel foam (size: 1 cm^2, thickness: 2 mm) as the work electrode, respectively. The detailed electrode fabrication was descripted as blow. Ag/AgCl (saturated KCl) electrode and platinum sheet were used as the reference and counter electrode, respectively. A 2 M KOH solution was used as the electrolyte. Cyclic voltammograms (CV) were measured within the potential range from 0.0 to 0.5 V at scan rates of 5, 10, 20, 50 and 100 mV s^{-1}, respectively. The galvanostatic charge-discharge test was carried out within a potential window from 0.10 to 0.45 V at different current densities of 0.5, 1.0, 2.0, 3.0, 4.0 and 5.0 A g^{-1}, respectively. The long-term cycle stability of cobalt oxide electrode was evaluated by the galvanostatic charge-discharge measurement at the current density of 1 $A \cdot g^{-1}$ in 2 M KOH aqueous solution.

Fabrication of Electrodes. Typically, 8 mg CoO (or Co_3O_4) powder, 1 mg acetylene black as the conducting agent and 50 ml polyvinylidone fluoride (PVDF) as a binder were homogeneously mixed with a few drops of ethanol in an agate mortar until a homogeneous black slurry was obtained. The resulting slurry was brushed into the nickel foam. The coated nickel foam was dried and pressed under a pressure of

10 MPa.

Results and Discussion

Synthesis Consideration. In this work, three isomeric benzenedicarboxylates, *o*-**bdc**, *m*-**bdc**, and *p*-**bdc**, were employed as ancillary ligands to perform a systematic study on the structure diversity of CPs based on the cobalt–**bibp** matrix. Evidently, three carboxylic ligands all possess two carboxylate groups, but exhibit various distributing positions on the phenyl ring. The rigid ligand **bibp** was chosen as the primary ligand owing to the fixed bidentate bridging mode, which makes it possible to focus on the effect of aromatic acid. Moreover, the linear **bibp** ligand usually leads to high interpenetration because of the long spacer.[14] With the concept of mixed-ligand frameworks in mind, we employed three above benzenedicarboxylates as ancillary ligands to construct CPs **1**-**3** with different dimensional architectures.

CPs **1**-**3** were all synthesized from the solvothermal methods. It is worthy to note that the reaction conditions have great differences, especially the solvent agents and temperatures. **1** was prepared under a CH_3CN-H_2O system at 125 °C. Under the similar conditions but using *m*-H_2**bdc** to replace *o*-H_2**bdc**, only a muddy substance was obtained. So we continued to change the organic solvent at the fixed ratio of 4:3 to water, and the temperature was kept rising at the step of 10 °C. However, when the temperature up to 185 °C, there is still no suitable crystals for single crystal X-ray diffraction by employing a wide range of organic solvents, such as CH_3OH, C_2H_5OH and $(CH_3)_2NCHO$. Fortunately, when a little ammonia water was added into the C_2H_5OH-H_2O system at 185 °C, high quality block crystals of **2** were isolated. **3** was also successfully synthesized through plenty of tentative experiments, which was well crystallized in the C_2H_5OH-H_2O system at 165 °C. The above statement shows how a variety of synthetic strategies for the generation of a series of CPs, and could be adapted to each particular reaction system.

For the synthesis of cobalt oxide particles, a facile and controllable approach was employed in our experiment. Firstly, CoO particles were prepared by the simple thermolysis of crystals of **1** under N_2 gas flow via a calcination treatment. However, when the air including O_2 gas was introduced into the calcination system, another cobalt oxide Co_3O_4 was successfully prepared. The result shows that the gas environment plays an important role in the formation of oxide particles.

Crystal Structure of 1. CP **1** crystallizes in the monoclinic space group $P2_1/c$ with six crystallographically independent Co^{II} ions in the asymmetric unit (Figure **1**). There are two coordination symmetries for the metal center, i.e. the tetrahedron and octahedron. The Co1, Co3 and Co5 ions lie in a

tetrahedral coordination environment, which are coordinated by three carboxylic O atoms of distinct *o*-**bdc**$^{2-}$ ions and one **bibp** N atom. However, the Co2, Co4 and Co6 ions lie in an octahedral coordination environment, which are coordinated by five carboxylic O atoms from three *o*-**bdc**$^{2-}$ ions (Particularly for the Co6 ion, one *o*-**bdc**$^{2-}$ O atom is displaced by one water molecule) and one **bibp** N atom. The coordination bond lengths that involve the metal center widely range from 1.933(4) to 2.193(4) Å for the Co–O bonds, whereas a narrow range [2.000(4)-2.088(4) Å] for the Co–N bonds (Table **S1**), which are all comparable to those typically observed values.[15] The coordination angles of tetrahedral or octahedral node span a wide range ([94.64(16)-130.10(16)º] and [60.00(12)-177.74(14)º], respectively), which illustrates that the Co^{II} ion has a distorted tetrahedral or octahedral coordination geometry.

(Insert Figure **1**)

The carboxylate group adopts four different coordination modes, i.e. the syn-syn, syn-anti, bidentate chelate and monatomic modes. Then the *o*-**bdc**$^{2-}$ ion takes three bridging patterns ((κ^1-κ^0)-(κ^1-κ^1)-μ_2, (κ^2)-(κ^1-κ^1)-μ_3 and (κ^1-κ^1)-(κ^1-κ^1)-μ_3) to connect the cobalt ion into a 1D chain (Figure **2a**).[16] Owing to various bridging modes of *o*-**bdc**$^{2-}$ ion, there are five kinds of magnetic coupling pathways mediated by the carboxylate group, with the Co–Co distances being about 3.81, 3.96, 4.40, 4.46 and 4.90 Å, respectively. Each **bibp** ligand, adopting a bidentate *trans*-coordinated conformation, connects two metal centers from diverse carboxylate∩cobalt chains. As a result, two neighboring 1D chains are bridged by the **bibp** ligand to give a 1D belt (Figure **2b**), which are further packed together to afford a 3D supermolecular architecture (Figure **S2**). The remaining space within this 3D supermolecular framework is occupied by the disordered CH_3CN molecule.

(Insert Figure **2**)

Crystal Structure of 2. Single-crystal X-ray diffraction analysis reveals that **2** crystallizes in the triclinic space group *P*-1. The asymmetric unit consists of one crystallographically independent Co^{II} ion, one ***m*-bdc**$^{2-}$ ion and one **bibp** ligand. As shown in Figure **3a**, the Co^{II} ion lies in a distorted octahedral coordination environment, which is surrounded by two monodentate carboxylic groups from distinct *m*-**bdc**$^{2-}$ ions, one bidentate chelate carboxylic group, and two imidazole rings of individual **bibp** ligands. The coordination bond lengths span from 2.0342(15) to 2.1973(16) Å for Co–O bonds, whereas 2.1405(18) and 2.1462(17) Å for Co–N bonds, which are all comparable to the above corresponding values.

(Insert Figure **3**)

The fully-deprotonated *m*-**bdc**$^{2-}$ ion bridges the Co^{II} ion to form a 1D double-track chain by employing

two carboxylic groups with different coordination modes, i.e. the bidentate chelate and syn-anti modes (Figure **3b**). Obviously, the 1D chain contains a binuclear cluster, which is bridged by two syn-anti carboxylate groups. It is worth mentioning that the Co1–O1–C25–O2–Co1$^{\#}$ (symmetry mode: -x+1, -y+1, -z+1) skeleton appreciably deviates from planarity [[dihedral angle between the planes Co1–O1–C25 and Co1$^{\#}$–O2–C25: 82.82(28)°], which plays a relevant role in the magnetic behavior. The bidentate ligand **bibp**, adopting a *trans*-coordinated conformation, connects two nodes from two neighboring 1D chains. As a result, the 1D chain is bridged by the **bibp** ligand to form a 2D extended layer (Figure **4**). If the binuclear unit was considered as a node, and both *m*-**bdc**$^{2-}$ and **bibp** ligands were viewed as linear linkers, then the topological simplification affords a 2D double-bridging (4,4) lattice.

(Insert Figure **4**)

Crystal Structure of 3. CP **3** crystallizes in the orthorhombic space group *Pnna* with one crystallographically independent Co^{II} ion located on the inversion center. As shown in Figure **5a**, the Co^{II} ion holds the CoO_2N_2 distorted tetrahedral coordination geometry, which is provided by two *p*-**bdc**$^{2-}$ oxygen atoms, and two **bibp** nitrogen atoms. The Co-O/N bond lengths are 1.9781(15) and 2.0355(19) Å respectively, in accord with the above reported values.

(Insert Figure **5**)

The *p*-**bdc**$^{2-}$ ion connects the metal ion into a 1D W-type chain with two monodentate carboxylate groups. The 1D chain is further connected by the *cis*-coordinated **bibp** ligand to form a 3D framework in a criss-cross mode (Figure **5b** & **S3**). The topological method was applied to explore the nature of this fascinating structure. The *p*-**bdc**$^{2-}$ and **bibp** ligands were viewed as linear linkers, and thus the Co^{II} ion could be simplified as a 4-connected node. Topological analysis performed on TOPOS Software gives a uninodal 4-connected network with the point symbol of $6^5\cdot8$ topology and long vertex symbol of $[6\cdot6\cdot6\cdot6\cdot6_2\cdot8_3]$,[17] which is topologically identical to the unusual ***dmp*** net (Figure **6**). Obviously, the ***dmp*** net is different from other 4-connected types: the well-known ***dia*** (6^6),[18] ***NbO*** $(6^4\cdot8^2)$,[19] ***PtS*** $(4^2\cdot8^4)$[20] and so on. It is worth noting that the present ***dmp*** net is closely related to the ***cds*** net.[21] Both of them have the same Schläfli symbol of $6^5\cdot8$, but with different vertex symbols ($6\cdot6\cdot6\cdot6\cdot6_2\cdot8_3$ for the ***dmp*** net, and $6\cdot6\cdot6\cdot6\cdot6_2\cdot8_2$ for the ***cds*** net). Notably, the ***cds*** net is based on the square node, and two neighboring layers are orthogonal. However, the ***dmp*** net is based on the tetrahedral node, which is a little similar to the 4-connected node of ***dia*** net, but the 8-membered circuit exists in the ***dmp*** net (being absent for the ***dia*** net). To the best of our knowledge, **3** shows the first example of ***dmp*** topology exclusively based upon the coordination bonds.

(Insert Figure **6**)

Because of large scale edges provided by the bulky building blocks *p*-**bdc**$^{2-}$ and **bibp**, the ***dmp*** framework illustrates a quadrangular chiral channel with the dimension of approximately 11.0 × 17.2 Å^2 along the *c* axis (Figure **S4**). However, these 1D channels are packed in an antiparallel manner with different chirality to cause an achiral CP, which is also indicated by the centrosymmetric space group *Pnna*. The potential void space provided by these 1D channels is destroyed by the interpenetration of three independent equivalent frameworks interlocked with each other. Thus, as we are aware, **3** represents an unprecedented three-fold interpenetrating ***dmp*** network (Figure **7**).

(Insert Figure **7**)

Effects of Orientation of Carboxylate Groups. CPs **1**-**3**, constructed from three structurally related aromatic dicarboxylic acids and the **bibp** ligand, illustrate 1D, 2D and 3D architectures based on heteroleptic Co^{II} nodes, respectively. In these mixed-ligand structures, the **bibp** ligand shows an invariable bidentate bridging mode, which facilitates us to perform a systematic study on the effect of benzoate. Interestingly, all three aromatic acids possess two carboxylate groups, which are deprotonated to participate in the construction of CPs. Thus, the title research could be focused on the orientation of carboxylate group, which is close related to the shape of aromatic acid. To elucidate the effect of benzenedicarboxylate on the topological structure, we assume the parameter φ as the angle between two carboxylate vectors.

The *o*-**bdc**$^{2-}$ ion with φ = 60º is employed in **1**. The Co^{II} ion illustrates two coordination symmetries (tetrahedron and octahedron), and the *o*-**bdc**$^{2-}$ ion adopts three bridging patterns ((κ^1)-(κ^1-κ^1)-μ_2, (κ^2)-(κ^1-κ^1)-μ_3 and (κ^1-κ^1)-(κ^1-κ^1)-μ_3) via two *o*-COO$^-$ groups. In such a way, the Co^{II} ion and *o*-**bdc**$^{2-}$ ligands are assembled into a 1D carboxylate∩cobalt chain with short distances in the range of 3.81-4.90 Å for two neighboring Co^{II} centers (Chart **1**). Furthermore, only one free coordination site is available for each metal ion in the 1D chain. The **bibp** ligand occupies the free site with a terminal N atom, and thus each bidentate **bibp** ligand bridegs two carboxylate∩cobalt chains to form a 1D belt. In **2**, the aromatic acid have two *m*-COO$^-$ groups with φ = 120º, which adopts a bidentate chelate and syn-anti mode, respectively. The octahedral Co^{II} ion is bridged by the *m*-**bdc**$^{2-}$ ion to form a 1D double-track chain. The carboxylate∩cobalt chain contains a binuclear cluster with the Co···Co distance of 4.34 Å, while other intrachain neighboring metal centers are 7.09 or 10.05 Å apart. Moreover, two free coordination sites of each Co^{II} ion are available for the **bibp** ligand, and therefore the 1D chain is extended by the bidentate ligand into a 2D double-bridging (4,4) lattice based on the binuclear unit. Referring to **3**, four coordination

sites of the tetrahedral Co^{II} node are shared by the *p*-**bdc**$^{2-}$ and **bibp** ligands. The aromatic acid possesses two *p*-COO^- groups with φ = 180º, which use the monatomic mode to connect the Co^{II} ion into a 1D W-type chain $[Co(p\text{-}\mathbf{bdc}^{2-})]_\infty$ with the shortest Co···Co distance of 10.98 Å. Meanwhile, another 1D chain $[Co(\mathbf{bibp})]_\infty$ is also formed. Then the assembly of above two kinds of 1D chains affords an unusual ***dmp*** net. Further inspection shows that the ***dmp*** framework presents a quadrangular channel, which is large enough to allow such three equivalent frameworks entangled with each other to form an unprecedented three-fold interpenetrating ***dmp*** network.

(Insert Chart **1**)

The results indicate that the orientation of carboxylate group plays an important role in the assembly of mixed-ligand frameworks. The angle φ directly determines the distance of two carboxylate groups. The smaller of φ value, two COO^- groups get closer, which is contributed to the formation of polynuclear units. In **1**, two COO^- groups of *o*-**bdc**$^{2-}$ ion are neck to neck, and the angle φ = 60º is the smallest among those of three aromatic acids. Two COO^- groups could chelate one Co^{II} ion to yield a seven-atom ring, which is impossible for other two benzenedicarboxylates. As a result, the assembly of *o*-**bdc**$^{2-}$ and Co^{II} ions gives a 1D magnetic chain, which could be considered as an infinite-nuclear unit. For **2**, two COO^- groups of *m*-**bdc**$^{2-}$ ion intersect with the angle of 120º, and the 1D carboxylate∩cobalt chain contains a magnetic binuclear cluster. The *p*-**bdc**$^{2-}$ ion has the angle of 180º, and two carboxylate groups exhibit the longest separation, which leads to the isolated Co^{II} ion in the carboxylate∩cobalt chain. Evidently, the rod-like building block *p*-**bdc**$^{2-}$ serves as the longest Co···Co edge comparing to *o*-**bdc**$^{2-}$ and *m*-**bdc**$^{2-}$, and thereby the ***dmp*** framework in **3** presents a 1D quadrangular channel. The potential void space is large enough for three equivalent ***dmp*** frameworks interlocked with each other. Therefore, the φ angle with a big value is apt to cause interpenetration.

Thermogravimetric Analysis. The thermal stability of CPs **1**-**3** has been determined by the TG analysis (Figure **S5**). The TG plot of **1** illustrates two steps of weight loss. In the first region of 71-197 ºC, it lost all solvent molecules (the free acetonitrile and coordinated water molecules: 3.6% obsd; 3.5% calcd). Upon further heating, the material lost weight continuously. From 338-476 ºC, the TG trace showed a sharp decline to give a weight decrease of 75.4 %, corresponding to the complete loss of organic ligand (76.7% calcd). The final mass remnant of 21.0% was consistent with decomposition of CoO (19.8% predicted). Comparing to **1**, CPs **2** and **3** contain no solvent molecules, and show only one step of weight loss. The mass of **2** remained largely unchanged until the decomposition onset temperature of 316 °C. All removal of

organic ligand was completed at 492 °C, indicated by a further weight loss of 86.4% (85.3% calcd). The final mass remnant of 13.6% was very close to that predicted for CoO (14.7%). The thermal stability of **3** was slightly greater than **2**, with an onset temperature for degradation of 323 °C. The quick weight loss of 86.2% was complete at 479 °C, corresponding to the full decomposition of **3**. The final mass remnant of 13.8% was indicative of CoO (14.7% calcd).

Magnetic Properties. In order to confirm the phase purity of bulk material, XRD experiments have been carried out. The XRD experimental and computer-simulated patterns are shown in Figure **S6**. The experimental patterns of **1**-**3** are in good agreement with the corresponding simulated ones, indicating that as-grown crystals are homogeneous. Then the variable temperature magnetic susceptibility data (χ) of **1** and **2** were measured on the crushed crystals under 1 kOe in the range of 2-300 K.

The molar direct-current magnetic susceptibilities of **1** are shown in Figure **8a**. At room temperature, the $\chi_m T$ value per formula is 17.18 $cm^3 \cdot K \cdot mol^{-1}$, significantly higher than the spin-only value expected for six isolated Co^{II} ions with S = 3/2 (11.25 $cm^3 \cdot K \cdot mol^{-1}$; g = 2.0). It gives a realistic g_{Co} value of 2.47 if we assume that the ions are uncoupled, which is attributed to the significant contribution from the unquenched orbital momentum in the octahedral field (the $^4T_{1g}$ state). Upon temperature cooling, the $\chi_m T$ curve monotonously decreases to a value of 5.04 $cm^3 \cdot K \cdot mol^{-1}$ at 2.0 K, which infers dominant antiferromagnetic interactions between Co^{II} ions; meanwhile, spin-orbital coupling effects may also influence the overall profile.[22] The data above 50 K follow the Curie-Weiss law with C = 18.55 $cm^3 \cdot K \cdot mol^{-1}$ and θ = -24.67 K. The large C value compared with the spin-only value indicates significant contribution from orbital momentum, and the medium negative θ value can be indicative of an overall antiferromagnetic coupling.

According to the structure of **1**, the system can magnetically be treated as a 1D carboxylate∩cobalt chain in which magnetic coupling is mediated through the carboxylate group. The inter-chain magnetic interaction through the rod-like ligand **bibp** is so weak that the coupling can be negligible. In the 1D chain, there are five kinds of magnetic coupling pathways with different Co···Co distances mediated by the carboxylate groups. Consequently, at least five J parameters are needed to fully mode the magnetic behavior. Besides, several parameters, such as λ (spin-orbital coupling parameter), α (orbital reduction factor) and Δ (axial distortion factor), are needed to account for the influences of single-site factors on the octahedral Co^{II} ion.[23] More terribly, the title 1D chain contains two different Co^{II} ions, one octahedron and the other tetrahedron. For the tetrahedral Co^{II} ion, the orbitally non-degenerate $^4A_2$ ground state experiences no first-order spin-orbital coupling. Instead, a true spin of 3/2 with g significantly deviating from 2.0 should

be considered.[24] Thus, there are no reliable models to quantitatively analyze the strength of magnetic exchange interactions in the complicated 1D system.

(Insert Figure **8**)

The magnetic susceptibility data of **2** are shown in Figures **8b** in the forms of χ_M and $\chi_M T$ vs T plot. The value of $\chi_M T$ at room temperature (6.13 $cm^3 \cdot K \cdot mol^{-1}$) is larger than the expected value for two isolated Co^{II} ions with S = 3/2 (3.75 $cm^3 \cdot K \cdot mol^{-1}$; g = 2.0). It gives a realistic g_{Co} value of 2.56 if we assume that the ions are uncoupled. As the temperature is lowered, the $\chi_M T$ value continues to decrease slowly, and reaches a minimum value of 4.59 $cm^3 \cdot K \cdot mol^{-1}$ at 12 K, after which a slight rise is observed. The variation of χ_M^{-1} vs T obeys the Curie-Weiss law in a rather high temperature range (300-60 K), giving a negative Weiss constant θ = -8.74 K and Curie constant C = 6.14 emu·K·mol^{-1}. The C value is as expected for the binuclear cluster.[25] It must be noted that the small negative θ constant is not necessarily indicative of antiferromagnetic interactions because the thermal magnetic behavior is strongly influenced by the spin-orbital coupling intrinsic to an octahedral Co^{II} ion. The spin-orbital coupling splits the $^4T_{1g}$ ground state into three Kramers levels: one sextet, quartet and ground doublet, respectively. Cooling the depopulation of above levels could cause a significant decrease for the $\chi_M T$ variation, which is associated with a negative θ constant (up to 20 K).[26] Therefore, the small θ constant may imply weak ferromagnetic coupling between metal ions, which is overcompensated by the effect of spin-orbital coupling above 12 K. The ferromagnetic coupling is also supported by the final increase at low temperatures (< 12 K).

According to the structure of **2**, the magnetic behavior is attributed to the binuclear cobalt cluster well-separated by long organic ligands, in which the magnetic coupling is mediated through two syn-anti−COO^- bridges. Consequently, to estimate the strength of ferromagnetic interactions (J) within the binuclear unit, an empirical approach proposed recently by Lloret et al was used to fit the experimental data.[27] In this approach, the Co^{II} ion is assumed to have an effective spin of S_{eff} = 1/2, which corresponds to the Kramers doublet and is related to the real spin (S = 3/2) by a factor of 5/3 (eqn (**1**)). The effective-spin Hamiltonian for the dinuclear Co^{II} system is described by eqn (**2**), and the magnetic susceptibility is expressed by eqn (**3**):

$$\hat{S} = (5/3)\hat{S}_{eff} \qquad \text{eqn (1)}$$

$$\hat{H} = -(25/9)J\hat{S}_{eff}^{A} \cdot \hat{S}_{eff}^{B} - G(T,J)\beta H(\hat{S}_{eff}^{A} + \hat{S}_{eff}^{B}) \qquad \text{eqn (2)}$$

$$\chi_{binuclear} = \frac{2N\beta[G(T,J)]^2}{KT}\frac{1}{3+\exp[(25/9)J/(KT)]} \qquad \text{eqn (3)}$$

where, $G(T, J)$ is a fictitious Landé factor dependent upon λ, α, Δ and J.

The best fit of experimental data leads to the following set of parameters: λ = -130.55 cm^{-1}, α = 1.35, Δ = -711.46 cm^{-1}, J = 1.28 cm^{-1} and $R = 1.03\times10^{-4}$ (R value is defined as $\sum[(\chi_M)_{obs}-(\chi_M)_{calc}]^2/\sum[(\chi_M)_{obs}]^2$). The values of parameters λ, α and Δ fall within the usual ranges expected for the six-coordinated Co^{II} complexes.[28] The low value of $|J/\lambda|$ ratio (0.01) supports the use of above empirical approach (this method is valid when $|J/\lambda| < 0.1$).[29] The obtained ferromagnetic coupling is in agreement with the well-known ability of the *syn-anti* carboxylate bridge to mediate weak ferromagnetic interactions.[30] For the *syn-anti* carboxylate mediator, magnetic orbitals are unfavorably oriented to produce a significant overlap and thus the ferromagnetic interaction is observed. In addition, the Co1–O1–C25–O2–$Co1^{\#}$ (symmetry mode: -x+1, -y+1, -z+1) skeleton appreciably deviates from planarity [the dihedral angle between planes Co1–O1–C25 and $Co1^{\#}$–O2–C25: 82.82(28)°]. The non-planarity of Co1–O1–C25–O2–$Co1^{\#}$ skeleton also reduces the overlap of magnetic orbitals and increases the ferromagnetic coupling.[31]

Electrochemistry Properties. Based on the TGA results, CP **1** exhibits good stability, but begins to decompose if heated up to about 330 °C. Fortunately, CoO and Co_3O_4 particles were prepared by the controllable calcination-thermolysis of crystals of **1**, and the XRD pattern tests were then performed (Figure **S7**). Two samples can be assigned to the face-centered cubic phase CoO and Co_3O_4, according to standard JCPDS cards no. 43-1004 and 65-3103, respectively. No impurity diffraction peaks were detected, indicating very high purity. The morphologies and microstructures of CoO and Co_3O_4 were investigated by SEM (Figure **S8**). Obviously, irregular particle agglomerates of CoO are observed, revealing that the as-synthesized CoO is actually composed of numerous microparticles, and these particles undergo further aggregation to form a porous block structure. However, the as-synthesized Co_3O_4 looks like much smaller, and presents nearly spherical nanoparticles with the sizes of 10-50 nm, which undergo further aggregation to form an agglomerate structure.

Figure **9** shows CV curves of CoO and Co_3O_4 electrodes at various scan rates. Both electrodes exhibit two pairs of well-defined redox peaks within the potential range of 0.0-0.5 V. Each pair of redox peaks corresponds to the reversible conversion between two different cobalt oxidation states. Thus, for both electrodes, the electrochemical process can be expressed as two sequential reactions:[32]

$$CoO + OH^- \leftrightarrow CoOOH + e^-; \qquad CoOOH + OH^- \leftrightarrow CoO_2 + H_2O + e^- \qquad (1)$$

$$Co_3O_4 + H_2O + OH^- \leftrightarrow 3CoOOH + e^-; \quad CoOOH + OH^- \leftrightarrow CoO_2 + H_2O + e^- \qquad (2)$$

Also seen from Figure **9**, the oxidation and reduction peaks shift continuously to higher and lower potentials, respectively. With increasing scanning rate, the potential separation between the oxidation and reduction peaks become wider due to the polarization of the electrode.[33] Figure **S9** shows the representative CV curves of CoO and Co_3O_4 electrodes at the scan rate of 5 $mV \cdot s^{-1}$, which suggest that the Co_3O_4 electrode storages higher charge than the CoO electrode.

Galvanostatic charge-discharge measurements of cobalt oxide electrodes were carried out at various current densities in a potential window of 0.10-0.45 V. The specific capacitance was calculated by the eqn (**4**):[34]

$$C = I\Delta t / \Delta V m \qquad \text{eqn (4)}$$

where C represents the mass specific capacitance, I the constant discharge current, Δt the discharging time, ΔV the voltage drop upon discharging, m the total mass of cobalt oxide powder. The capacitance values of CoO electrode are 45.3, 42.6, 37.1, 33.4, 29.7 and 25.7 $F \cdot g^{-1}$ at specific current densities of 0.5, 1.0, 2.0, 3.0, 4.0 and 5.0 $A \cdot g^{-1}$, respectively (Figure **10a**). The capacitance values of Co_3O_4 electrode are 104.7, 99.4, 89.1, 78.9, 69.7 and 57.1 $F \cdot g^{-1}$ at corresponding current densities, respectively (Figure **10b**). It is noted that the capacitance values decreased with increasing current density, which is mainly attributed to the insufficient faradic redox reaction arising from the surface reduction by the OH^- ion under high discharge current density.[35] The specific capacitance at these current densities for two electrodes was calculated and compared (Figure **11**). The Co_3O_4 electrode always exhibits higher specific capacitance; its discharge specific capacitance is measured to be 104.7 $F \cdot g^{-1}$ at 0.5 $A \cdot g^{-1}$, more than two times of that of the CoO electrode (45.3 $F \cdot g^{-1}$).

Both the voltammogram and charge-discharge measurements show that the Co_3O_4 electrode storages higher charge than the CoO electrode, which has more potential to be used as the electrode material of electrochemical capacitor. At the same time, the Co_3O_4 electrode exhibits excellent long-term cycle life and high reversibility over entire cycle numbers (Figure **12**), and the capacitance decreased only 11.7 % of initial capacitance after 2500 cycles. The excellent cycle stability of Co_3O_4 electrode is ascribed to the large surface area and dense reaction site, which can significantly improve the utilization and capacitance of active material, provided by the effective mesoporous structure of the Co_3O_4 electrode.[36]

Conclusion

Three novel CPs **1**-**3** based on the cobalt–**bibp** matrix have been successfully synthesized via incorporation of three benzenedicarboxylates. Owing to the different orientations (φ) of carboxylate groups, the benzoates adopt various bridging modes to connect metal centers into diverse carboxylate∩cobalt chain-like architectures with 1D chain, binuclear and single-ion magnetic units, respectively. The metal nodes lying on these 1D architectures are further decorated by the **bibp** ligand to afford 1D, 2D and 3D mixed-ligand frameworks, respectively. Interestingly, **3** represents an unprecedented three-fold interpenetrating ***dmp*** network. Thereby the orientation of carboxylate group controls over the structure of mixed-ligand framework: the small value of φ is liable to form the polynuclear unit, while the large is beneficial to the highly dimensional and interpenetrating framework. Furthermore, the research on the magnetic property shows the antiferromagnetic coupling in **1**, and the ferromagnetic coupling constant of **2** is estimated by fitting the experimental data. Significantly, CoO and Co_3O_4 particles were obtained from the gas-controllable calcination-thermolysis of crystals of **1**, which appear as micro- or nanoparticles and have the potential as the electrode material of supercapacitor.

Acknowledgment. This work was supported by the National Natural Science Foundation of China (21103138), New teacher fund of doctorial program sponsored by Ministry of Education of China (20116101120023), and Natural Science Foundation of Shannxi (2014JQ2057, 2013JK0672, 14JS007).

Supporting Information Available: X-ray crystallographic data for complexes **1**-**3** in CIF format, selected bond lengths and angles, additional plots in WORD format, IR figures, TG figures, XRD figures, SEM images and representative CV curves. This material is available free of charge via the Internet at http://pubs.rsc.org.

References

(1) http://en.wikipedia.org/wiki/Coordination_polymers, and references therein.

(2) (a) Vukotic, V. N.; Loeb, S. J. *Chem. Soc. Rev.* **2012**, *41*, 5896; (b) Leong, W. L.; Vittal, J. J. *Chem. Rev.* **2011**, *111*, 688; (c) Tian, D.; Chen, Q.; Li, Y.; Zhang, Y. H.; Chang, Z.; Bu, X. H. *Angew. Chem. Int. Ed.* **2014**, *53*, 837; (d) Foo, M. L.; Matsuda, R.; Kitagawa, S. *Chem. Mater.* **2014**, *26*, 310; (e) Weng, D. F.; Wang, Z. M.; Gao, S. *Chem. Soc. Rev.* **2011**, *40*, 3157; (f) Zhang, J. P.; Zhang, Y. B.; Lin, J. B.; Chen, X. M. *Chem. Rev.* **2012**, *112*, 1001; (g) Zeng, M. H.; Yao, M. X.; Liang, H.; Zhang, W. X.; Chen, X. M. *Angew. Chem. Int. Ed.* **2007**, *46*, 1832; (h) Gros, C. R.; Peprah, M. K.; Hosterman, B. D.; Brinzari, T. V.; Quintero, P. A.; Sendova, M.; Meisel, M. W.; Talham, D. R. *J. Am. Chem. Soc.* **2014**,

136, 9846.

(3) (a) Li, Y. W.; Ma, H.; Chen, Y. Q.; He, K. H.; Li, Z. X.; Bu, X. H. *Cryst. Growth Des.* **2012**, *12*, 189; (b) Zhao, D.; Timmons, D. J.; Yuan, D. Q.; Zhou, H. C. *Acc. Chem. Res.* **2011**, *44*, 123; (c) Mereacre, V.; Baniodeh, A. C.; Anson, E.; Powell, A. K. *J. Am. Chem. Soc.* **2011**, *133*, 15335; (d) Du, M.; Li, C. P.; Liu, C. S.; Fang, S. M. *Coor. Chem. Rev.* **2013**, *257*, 1282.

(4) (a) Bagai, R.; Christou, G. *Chem. Soc. Rev.* **2009**, *38*, 1011; (b) Liu, R.; Li, L.; Wang, X.; Yang, P.; Wang, C.; Liao, D.; Sutter, J. P. *Chem. Commun.* **2010**, *46*, 2566; (c) Jiang, S. D.; Wang, B. W.; Sun, H. L.; Wang, Z. M.; Gao, S. *J. Am. Chem. Soc.* **2011**, *133*, 4730.

(5) (a) Joan Ribas, Coordination Chemistry, Wiley, Weinheim, 2008; (b) Zeng, Y. F.; Hu, X.; Liu, F. C.; Bu, X. He. *Chem. Soc. Rev.* **2009**, *38*, 469; (c) Kurmoo, M. *Chem. Soc. Rev.* **2009**, *38*, 1353.

(6) (a) Vallejo, J.; Castro, T.; Rafael, R. G.; Cano, J.; Julve, M.; Lloret, F.; Munno, G. De.; Wernsdorfer, W.; Pardo, E. *J. Am. Chem. Soc.* **2012**, *131*, 15704; (b) Juhász, G.; Matsuda, R.; Kanegawa, S.; Inoue, K.; Sato, O.; Yoshizawa, K. *J. Am. Chem. Soc.* **2009**, *131*, 4560; (c) Hayami, S.; Komatsu, Y.; Shimizu, T.; Kamihata, H.; Lee,Y. H. *Coor. Chem. Rev.* **2011**, *255*, 1981.

(7) The equation is proposed by Christou in this article: Christou, G. *Polyhedron,* 2**005**, *24*, 2065. Herein U is the energy barrier directly associated with T_b, S_T is the spin ground state, and D is the zero-field splitting gauging the axial anisotropy.

(8) (a) Bo, L.; Shioyama, H.; Akita, T.; Xu, Q. *J. Am. Chem. Soc.* **2008**, *130*, 5390; (b) Yang, S. J.; Kim, T.; Im, J. H.; Kim, Y. S.; Lee, K.; Jung, H.; Park, C. R. *Chem. Mater.* **2012**, *24*, 464; (c) Hu , M.; Belik, A. A.; Imura, M.; Mibu, K.; Tsujimoto, Y.; Yamauchi, Y. *Chem. Mater.* **2012**, *24*, 2698; (d) Cho, W.; Lee, Y. H.; Lee, H. J.; Oh, M. *Adv. Mater.* **2011**, *23*, 1720.

(9) (a) Zhang, L.; Wu, H. B.; Madhavi, S.; Hng, H. H.; Lou, X. W. *J. Am. Chem. Soc.* **2012**, *134*, 17388; (b) Xu, X. D.; Cao, R. G.; Jeong, S. Y.; Cho, J. *Nano Lett.* **2012**, *12*, 4988; (c) Cho, W.; Park, S.; Oh, M. *Chem. Commun.* **2011**, *47*, 4138.

(10) Fan, J.; Hanson, B. E. *Chem Commun*. **2005**, *18*, 2327.

(11) Bruker AXS: Madison, WI, *SAINT Software Reference Manua*l, **1998**.

(12) G. M. Sheldrick, *SHELXTL NT Version 5.1. Program for Solution and Refinement of Crystal Structures*; University of Göttingen: Germany. **1997**.

(13) Spek, A. L. *J. Appl. Cryst.,* **2003**, *36*, 7.

(14) (a) Li, Z. X.; Xu, Y.; Zuo, Y.; Li, L.; Pan, Q.; Hu, T. L.; Bu, X. H. *Cryst. Growth & Des.* **2009**, *9*, 3904;

(b) Li, Z. X.; Chu, X.; Cui, G. H.; Liu, Y.; Li, L.; Xue, G. L. *CrystEngComm.* **2011**, *13*, 1984.

(15) (a) Chen, Q.; Chang, Z.; Song, W. C.; Song, H.; Song, H. B.; Hu, T. L.; Bu, X. H. *Angew. Chem. Int. Ed.* **2013**, *52*, 11550; (b) Lin, W. Q.; Leng, J. D.; Tong, M. L. *Chem. Commun.* **2012**, *48*, 4477; (c) Yang, E. C.; Liu, Z. Y.; Liu, T. Y.; Li, L. L.; Zhao, X. J. *Dalton Trans.* **2011**, *40*, 8132; (d) Li, X. B.; Zhuang, G. M.; Wang, X.; Wang, K.; Gao, E. Q. *Chem. Commun.* **2013**, *49*, 1814; (e) Zhou, Y. L.; Zeng, M. H.; Wei, L. Q.; Li, B. W.; Kurmoo, M. *Chem. Mater.* **2010**, *22*, 4295.

(16) This kind of notation describes the bridging mode of organic ligand as (κ^{x1})-(κ^{x2})…-(κ^{xn})-μ_y, where y is the overall number of metal ions bound by the whole ligand, and each value of x refers to the number of metal ions attached to different donor atoms: (a) Karra, J. R.; Huang, Y. G.; Walton, K. S. *Cryst. Growth Des.* **2013**, *13*, 1075; (b) Liu, L.; Ding, J.; Huang, C.; Li, M.; Hou, H.; Fan, Y. T. *Cryst. Growth Des.* **2014**, *14*, 3035.

(17) Blatov, V. A.; Shevchenko, B. P.; Serezhkin, V. N. *J. Appl. Cryst.* **2000**, *33*, 1193.

(18) (a) Panda, T.; Pachfule, P.; Chen, Y. F.; Jiang, J. W.; Banerjee, R. *Chem. Commun.* **2011**, *47*, 2011; (b) Wang, F.; Tan, Y. X.; Yang, H.; Kang, Y.; Zhang, J. *Chem. Commun.* **2012**, *48*, 4842.

(19) (a) Gao, W. Y.; Chen, Y.; Niu, Y. H.; Williams, K.; Cash, L.; Perez, P. J.; Wojtas, L.; Cai, J. F.; Chen, Y. S.; Ma, S. Q. *Angew. Chem. Int. Ed.* **2014**, *53*, 2615; (b) Zhang, Z. M.; Yao, S.; Li, Y. G.; Clérac, R.; Lu, Y.; Su, Z. M.; Wang, E. B. *J. Am. Chem. Soc.* **2009**, *131*, 14600.

(20) (a) Chen, X. Y.; Huang, R. B.; Zheng, L. S.; Tao, J. *Inorg. Chem.* **2014**, *53*, 5246; (b) Murphy, M. J.; D'Alessandro, D. M.; Kepert, C. J. *Dalton Trans.* **2013**, *42*, 13308.

(21) (a) Li , G. B.; Li , L.; Liu, J. M.; Yang , T.; Su, C. Y. *Cryst. Growth Des.* **2013**, *13*, 1518; (b) Zhao, J. W.; Zheng, S. T.; Li, Z. H.; Yang, G. Y. *Dalton Trans.* **2009**, *8*, 1300.

(22) (a) Bryan, A. M.; Merrill, W. A.; Reiff, W. M.; Fettinger, J. C.; Power, P. P. *Inorg. Chem.* **2012**, *51*, 3366; (b) Wang, X. L.; Li, L. C.; Liao, D. Z. *Inorg. Chem.* **2010**, *49*, 4735.

(23) Fabelo, O.; Cañadillas-Delgado, L.; Pasán, J.; Delgado, F. S.; Lloret, F.; Cano, J.; Julve, M.; Ruiz-Pérez, C. *Inorg. Chem.* **2009**, *48*, 11342.

(24) Carlin, R. L.; Magnetochemistry, Springer-Verlag, Berlin, Heidelberg,**1986**.

(25) Niu, C. Y.; Zheng, X. F.; Wan, X. S.; Kou, C. H. *Cryst. Growth & Des.* **2011**, *11*, 2874.

(26) Jing, X. H.; Yi, X. C.; Gao, E. Q.; Blatov, V. A. *Dalton Trans.* **2012**, *41*, 14316.

(27) Lloret, F.; Julve, M.; Cano, J.; Ruiz-García, R.; Pardo, E. *Inorg. Chim. Acta.* **2008**, *361*, 3432.

(28) Ma, Y.; Li, X. B.; Yi, X. C.; Jia, Q. X.; Gao, E. Q.; Liu, C. M. *Inorg. Chem.* **2010**, *49*, 8092.

(29) Rodríguez-Diéguez, A.; Seco, J. M.; Colacio, E. *Eur. J. Inorg. Chem.* **2012**, *2*, 203.

(30) Wang, S.; Bai, J.; Xing, H.; Li, Y.; Song, Y.; Pan, Y.; Scheer, M.; You, X. *Cryst. Growth Des.* **2007**, *7*, 747.

(31) (a) Arora, H.; Lloret, F.; Mukherjee, R. *Dalton Trans.* **2009**, *44*, 9759; (b) Zeng, M. H.; Zou, H. H.; Hu, S.; Zhou, Y. L.; Du, M.; Sun, H. L. *Cryst. Growth Des.* **2009**, *9*, 4239.

(32) (a) Rakhi, R. B.; Chen, W.; Cha, D.; Alshareef, H. N. *Nano Lett.* **2012**, *12*, 2559; (b) Zhou, C.; Zhang, Y.; Li, Y.; Liu, J. *Nano Lett.* **2013**, *13*, 2078; (c) Keng, P. Y.; Bull, M. M.; Shim, I. B.; Nebesny, K. G.; Armstrong, N. R.; Sung, Y. H.; Char, K.; Pyun, J. *Chem. Mater.* **2011**, *23*, 1120.

(33) (a) Meher, S. K.; Rao, G. R. *J. Phys. Chem. C.* **2011**, *115*, 15646; (b) Jiang, J.; Liu, J.; Ding, R.; Ji, X.; Hu, Y.; Li, X.; Hu, A.; Wu, F.; Zhu, Z.; Huang, X. *J. Phys. Chem. C*. **2010**, *114*, 929.

(34) (a) Liu, J. W.; Essner, J.; Li, J. *Chem. Mater.* **2010**, *22*, 5022; (b) Dong, X. C.; Xu, H.; Wang, X. W.; Huang, Y. X.; Chan-Park, M. B.; Zhang, H.; Wang, L. H.; Huang, W.; Chen, P. *ACS Nano* **2010**, *6*, 3206.

(35) (a) Vu, A.; Li, X. Y.; Phillips, J.; Han, A.; Smyrl, W. H.; Bühlmann, P.; Stein, A. *Chem. Mater.* **2013**, *25*, 4137; (b) Yana, J.; Wei, T.; Qiao, W.; Shao, B.; Zhao, Q.; Zhang, L.; Fan, Z.; *Electrochimica. Acta*. **2010**, *55*, 6973.

(36) (a) Liang, K.; Tang, X.; Hu, W. *J. Mater. Chem.* **2012**, *22*, 11062; (b) Wei, T. Y.; Chen, C. H.; Chang, K. H.; Lu, S. Y.; Hu, C. C. *Chem. Mater.* **2009**, *21*, 3228.

Captions to Figures

Chart 1. A series of 1D carboxylate∩cobalt chains constructed from three structurally related aromatic dicarboxylic acids, which take different bridging modes.

Figure 1. View of the asymmetric unit, and coordination environments of Co^{II} ions in **1** (the O atoms cycled by the black ring are equivalent).

Figure 2. View of the (a) 1D carboxylate∩cobalt chain; (b) 1D belt in **1**.

Figure 3. View of the (a) coordination environment of Co^{II} ion; (b) 1D carboxylate∩cobalt chain containing a binuclear cluster in **2**.

Figure 4. The 2D double-bridging (4,4) layer based on the binuclear cluster in **2**.

Figure 5. View of the (a) coordination environment of Co^{II} ion; (b) 1D carboxylate∩cobalt chain, further connected by the **bibp** ligand into a 3D framework in **3**.

Figure 6. View of the $6^5 \cdot 8$ topology in **3** (the green and red rings denote the 6-membered and 8-membered circuits, respectively).

Figure 7. The three-fold interpenetrating ***dmp*** network.

Figure 8. Thermal dependence of χ_M^{-1}, χ_M, $\chi_M T$, and corresponding theoretical curves: (a) **1**; (b) **2**.

Figure 9. The CV curves at scan rates of 5, 10, 20, 50 and 100 $mV \cdot s^{-1}$: (a) CoO; (b) Co_3O_4.

Figure 10. Galvanostatic charge-discharge curves at different current densities: (a) CoO; (b) Co_3O_4.

Figure 11. The current density dependence of specific capacitance for the CoO and Co_3O_4 electrodes.

Figure 12. Average specific capacitance *versus* cycle number of the Co_3O_4 electrode at a galvanostatic charge-discharge current density of 1 $A \cdot g^{-1}$. Inset: first ten charge/ discharge curves of the Co_3O_4 electrode.

Table 1. Crystallographic Data and Structure Refinement Parameters for **1**-**3**.

Complex	**1**	**2**	**3**
Chemical formula	$C_{105}H_{72.5}Co_6N_{13.5}O_{25}$	$C_{26}H_{18}CoN_4O_4$	$C_{26}H_{18}CoN_4O_4$
formula weight	2276.84	509.37	509.37
crystal system	Monoclinic	Triclinic	Orthorhombic
space group	$P2_1/c$	P-1	$Pnna$
a (Å)	23.577(4)	9.990(4)	13.152(3)
b (Å)	21.515(4)	10.046(4)	17.365(4)
c (Å)	20.120(4)	11.176(5)	9.3149(19)
α	90	92.603(6)	90
β (deg)	112.540(3)	92.028(6)	90
γ	90	97.537(7)	90
V (Å^3)	9426(3)	1109.9(8)	2127.3(7)
Z	4	2	4
$D_{calcd.}$ (g cm^{-3})	1.604	1.524	1.590
μ (mm^{-1})	1.120	0.816	0.852
F(000)	4636	522	1044
reflns collected/unique	68562/23509	8467/5639	21021/2444
$R_{(int)}$	0.0461	0.0186	0.0527
$R_1{}^a$ [$I > 2\sigma(I)$]	0.0682	0.0345	0.0416
$wR_2{}^b$	0.2040	0.0939	0.0991
GOF	1.044	1.088	1.099
$\Delta_{\rho max}/\Delta_{\rho min}$ (e Å^{-3})	1.041/-0.734	0.331/-0.334	0.318/-0.284

$^a R = \Sigma||F_o| - |F_c|| / \Sigma|F_o|$; $^b R_w = [\Sigma[w(F_o^2 - F_c^2)^2] / \Sigma w(F_o^2)^2]^{1/2}$.

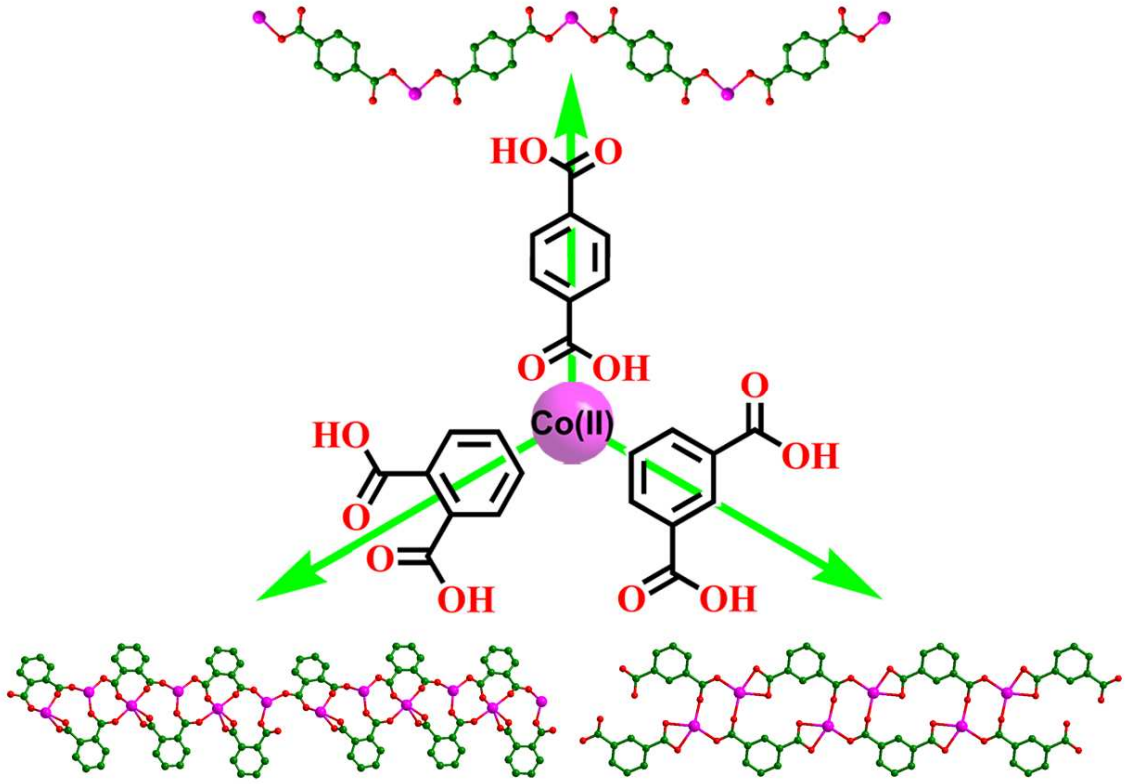

Chart 1

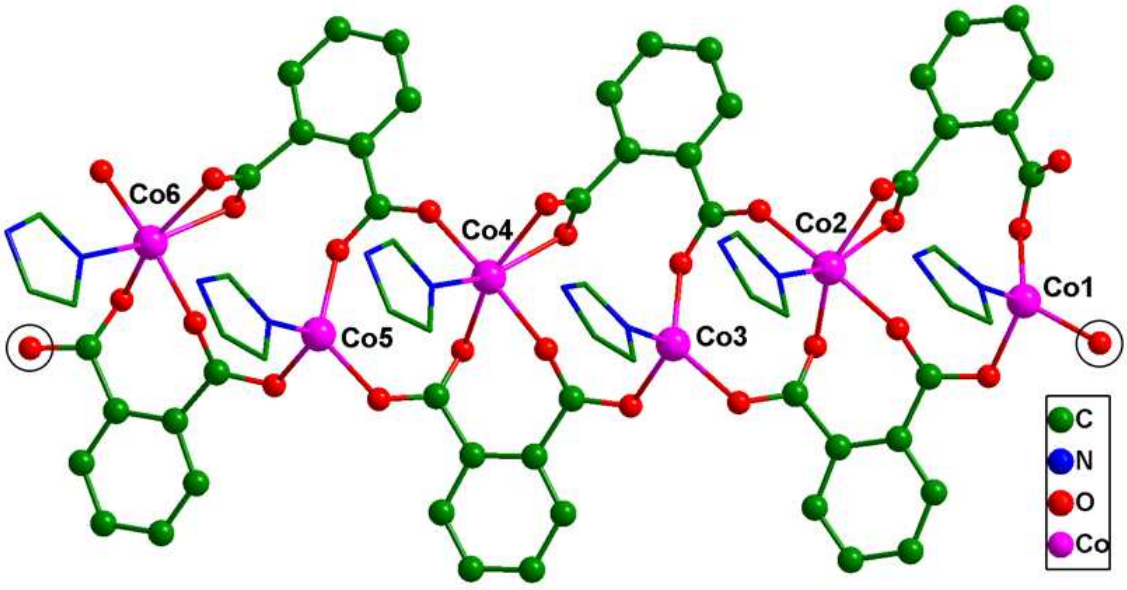

Figure 1

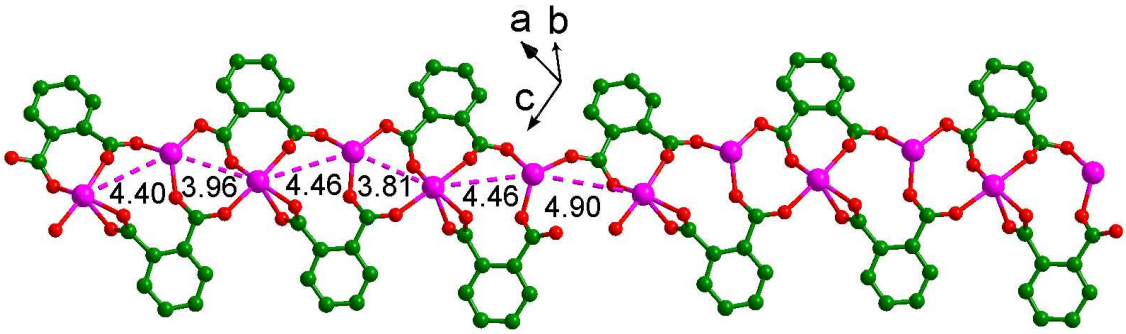

(a)

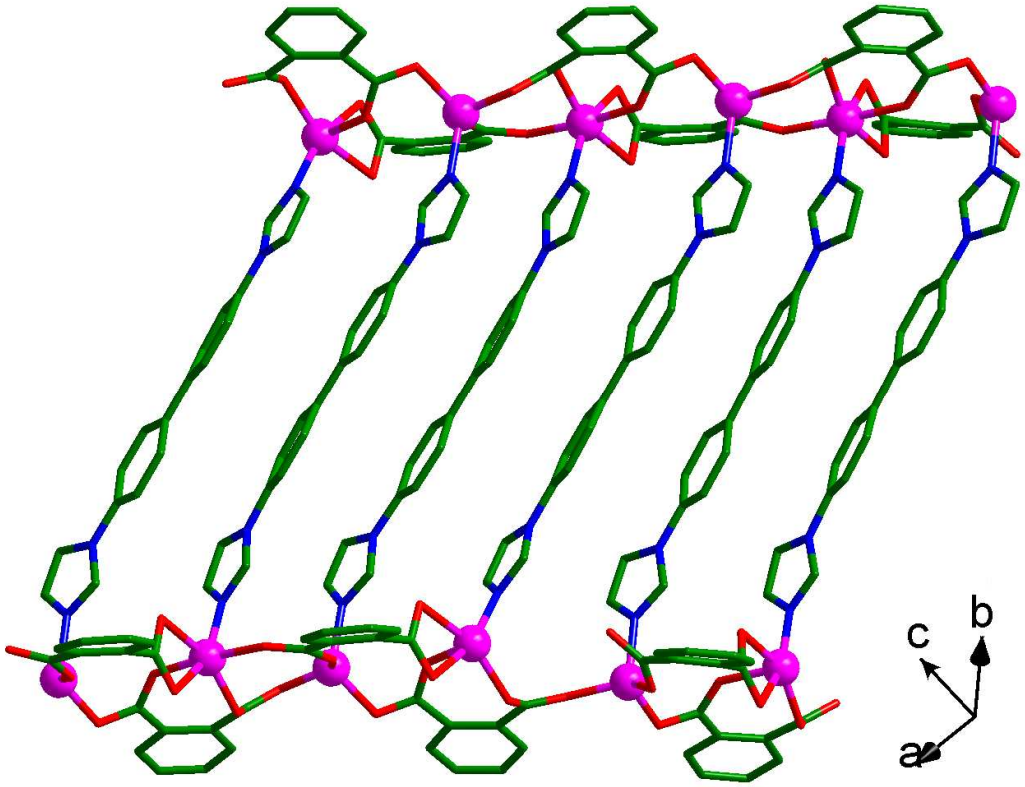

(b)

Figure 2

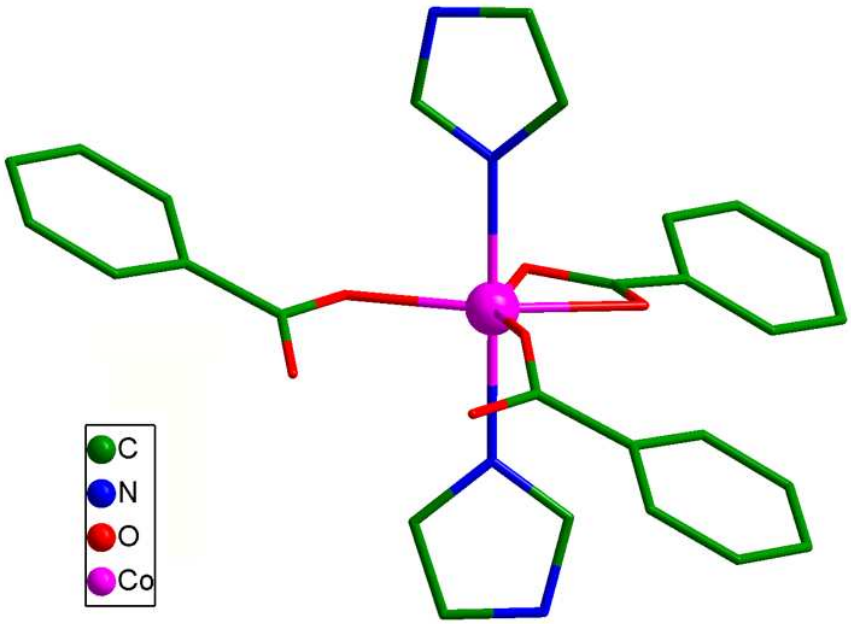

(a)

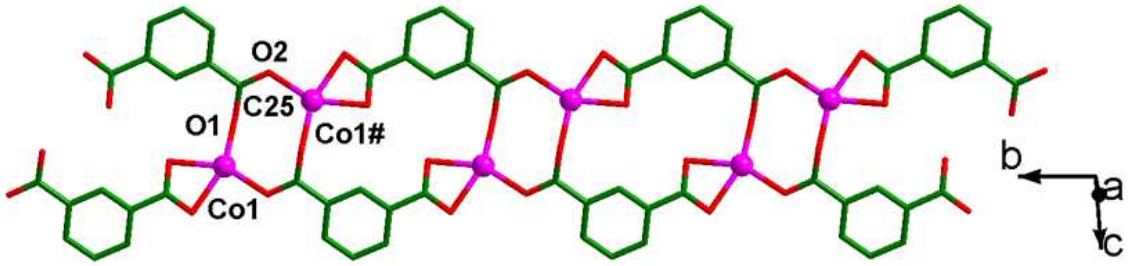

(b)

Figure 3

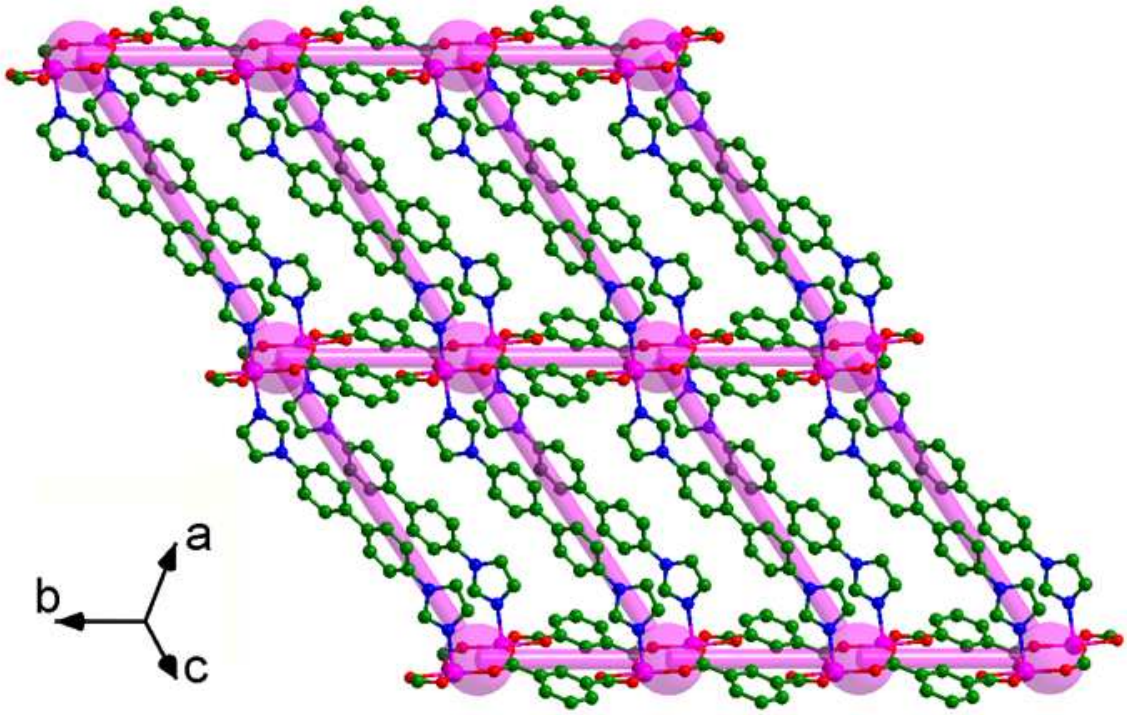

Figure 4

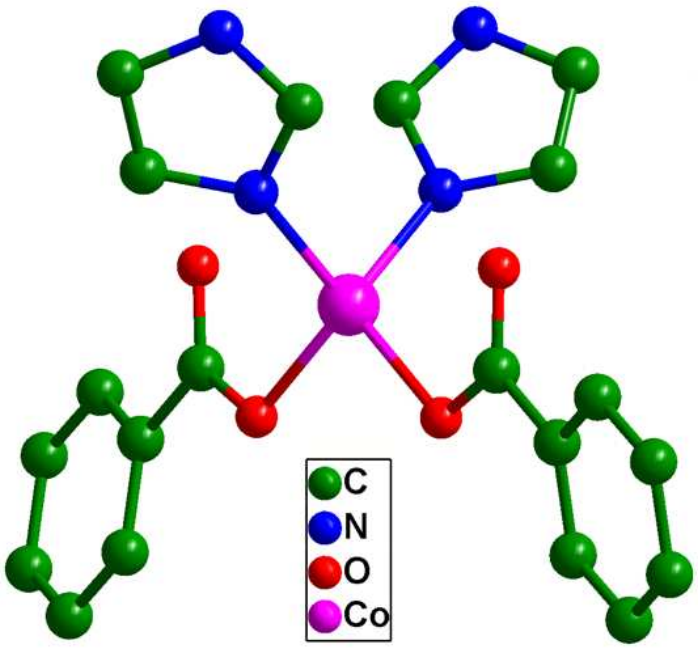

(a)

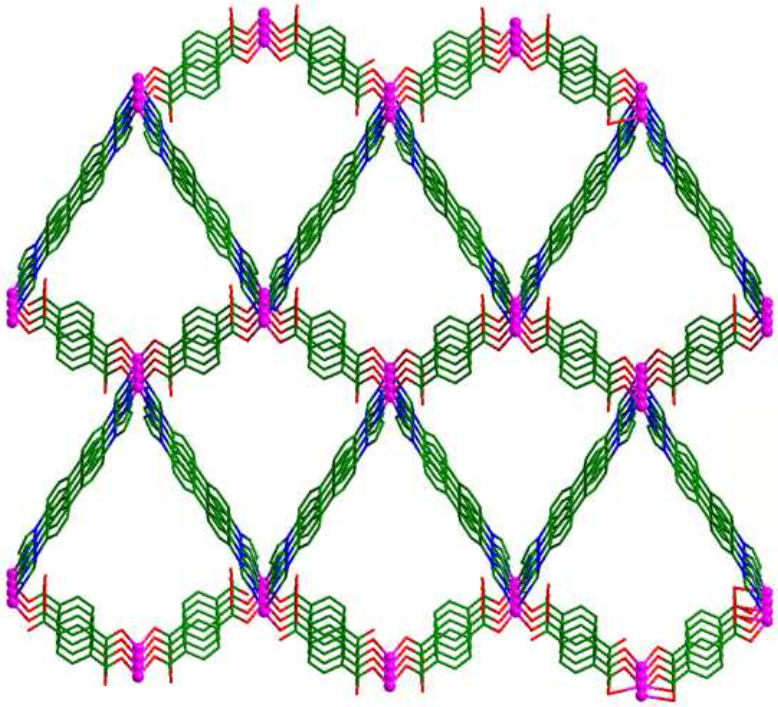

(b)

Figure 5

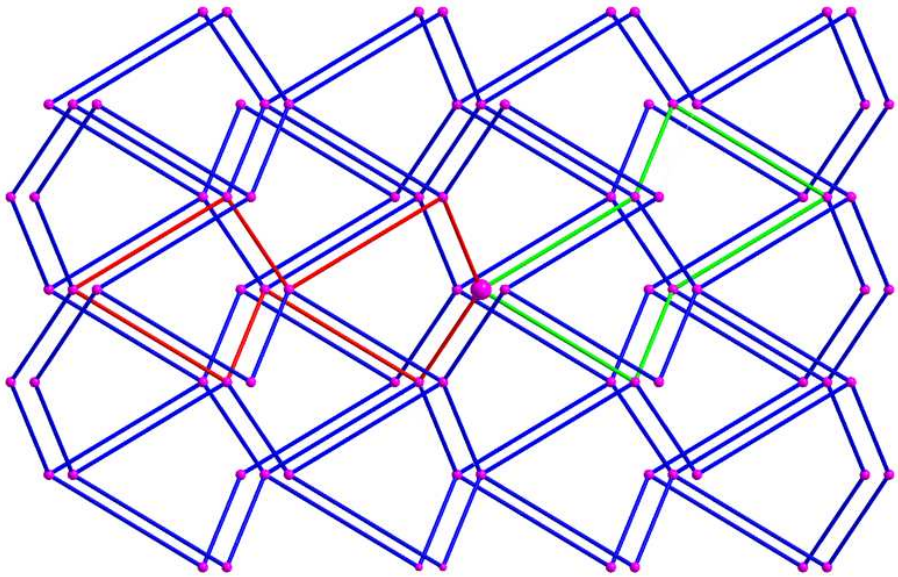

Figure 6

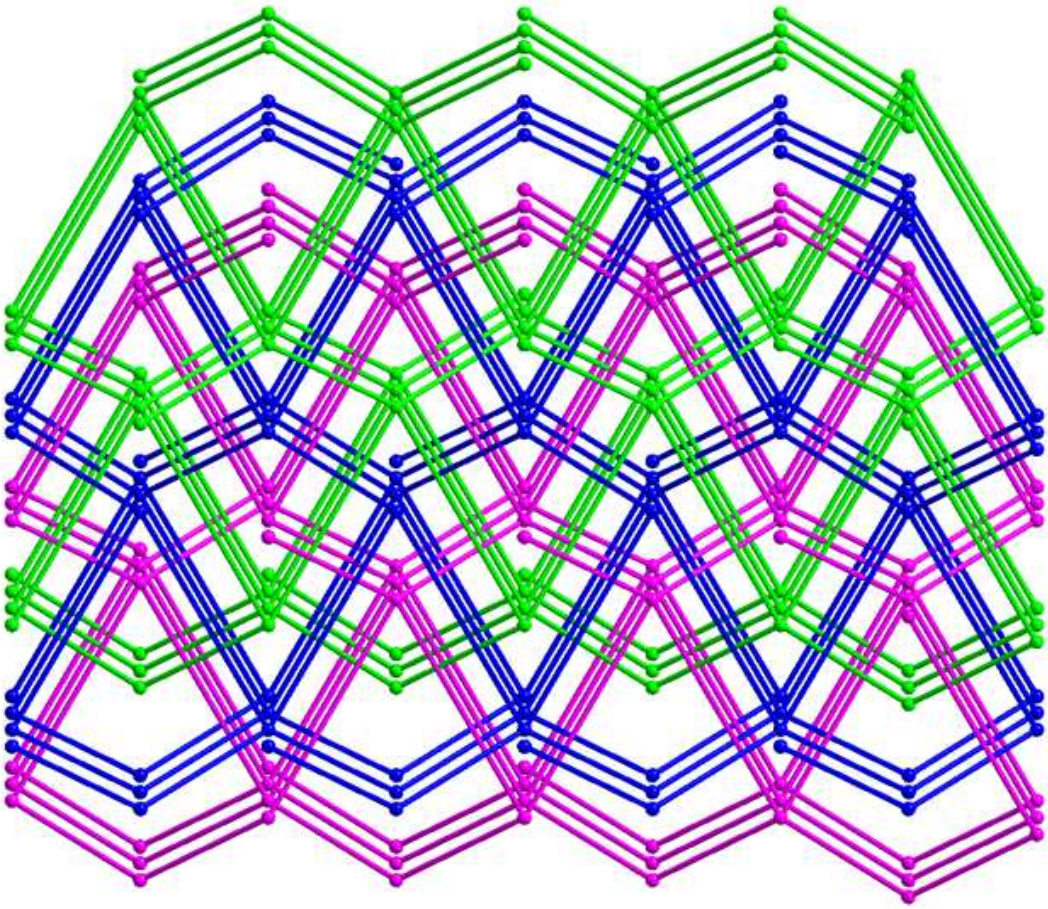

Figure 7

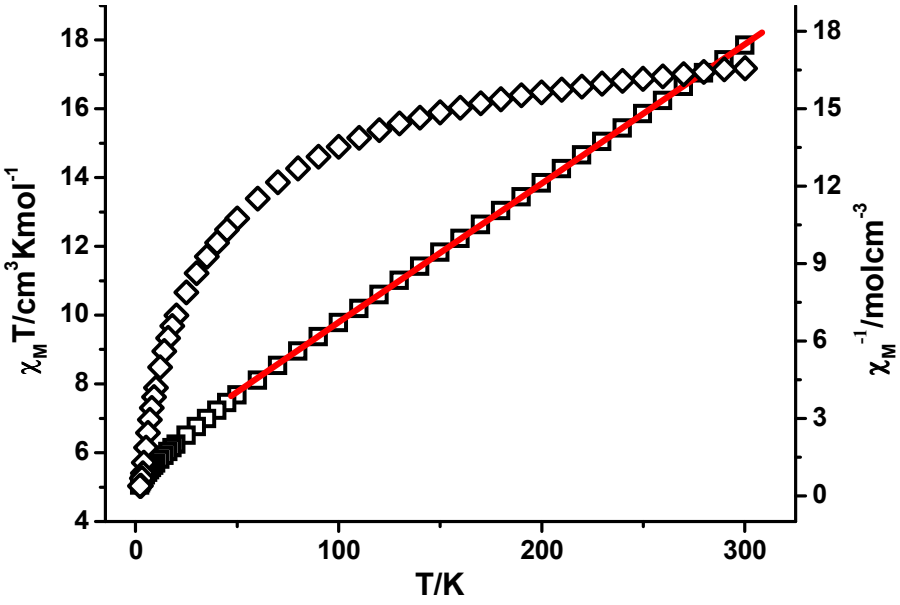

(a)

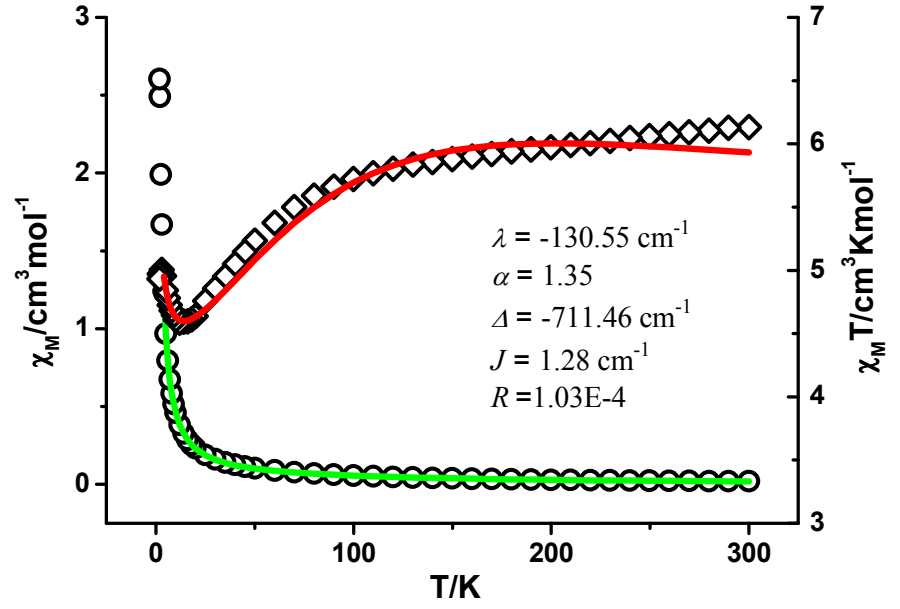

(b)

Figure 8

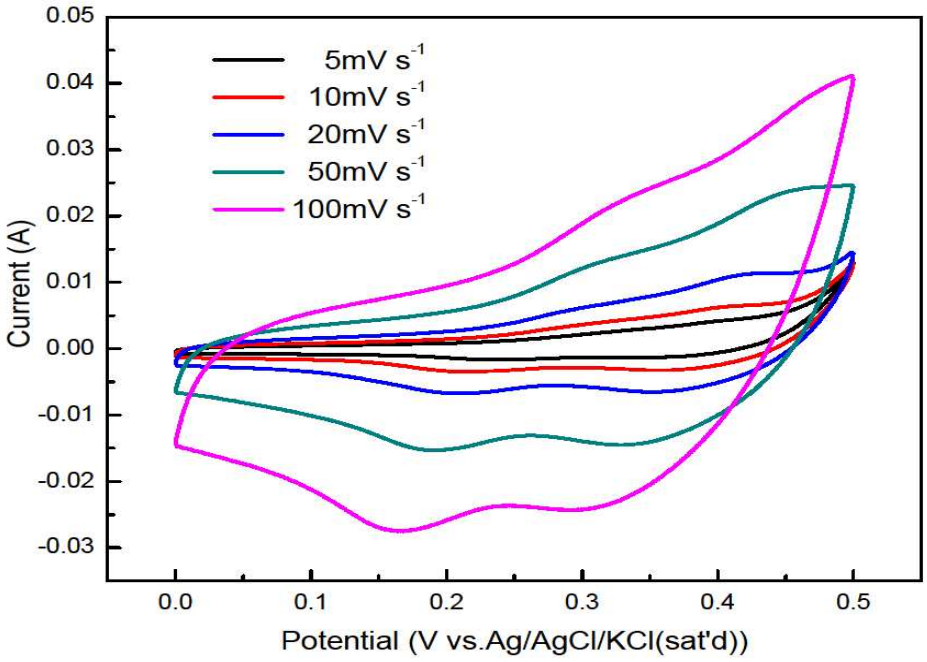

(a)

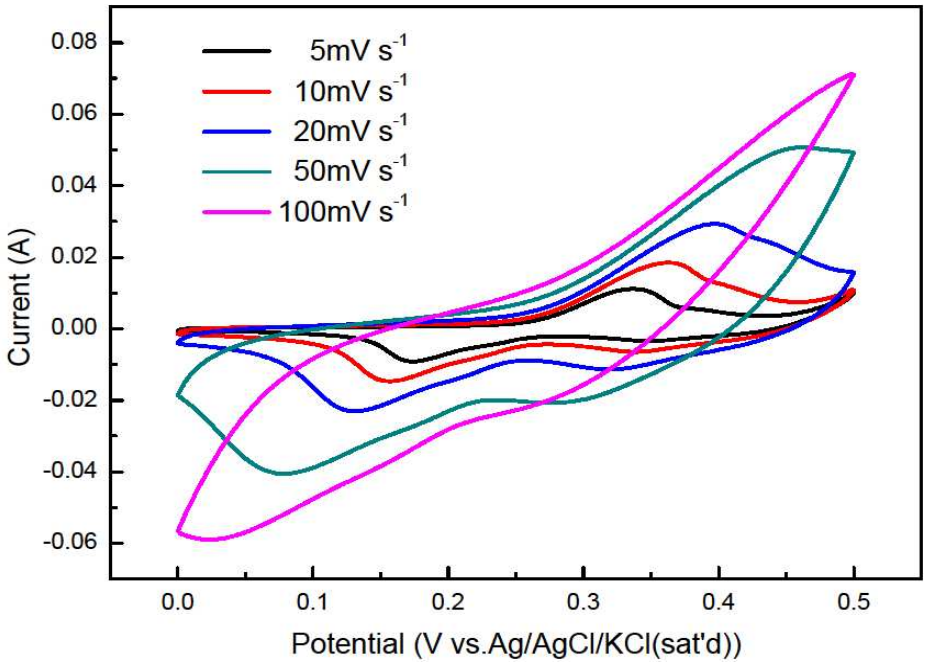

(b)

Figure 9

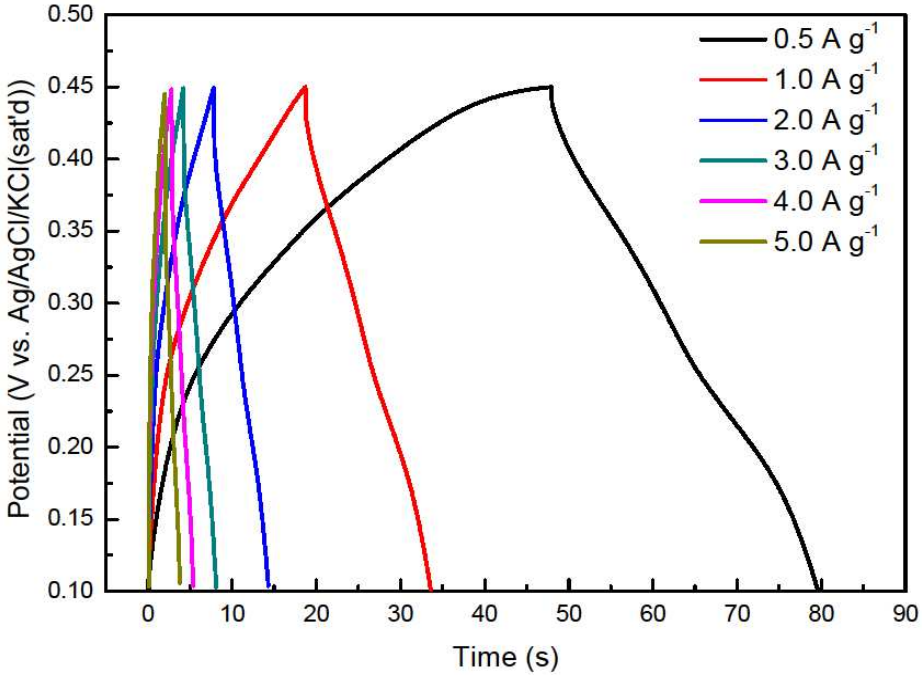

(a)

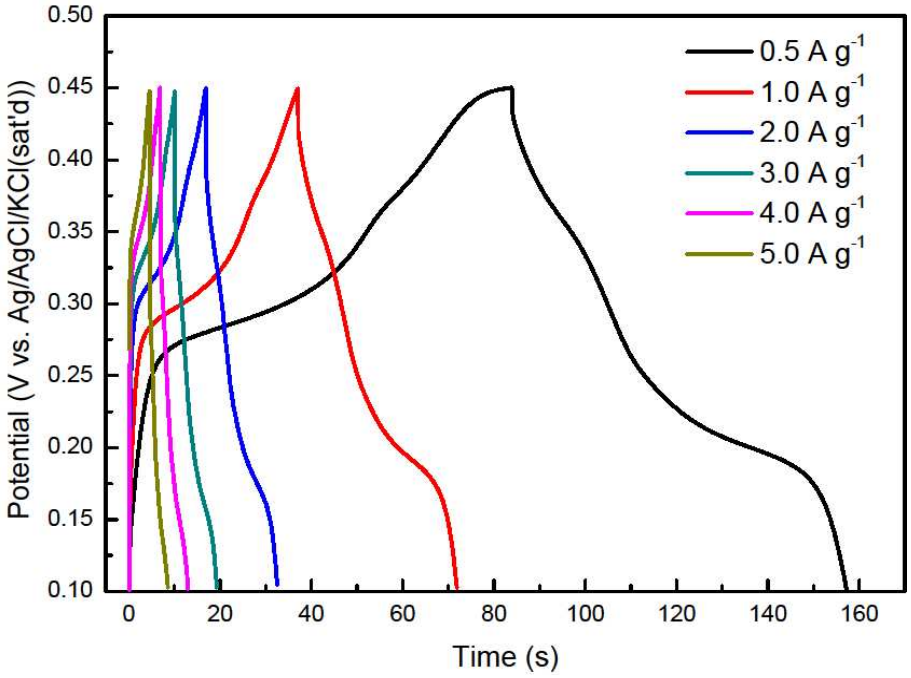

(b)

Figure 10

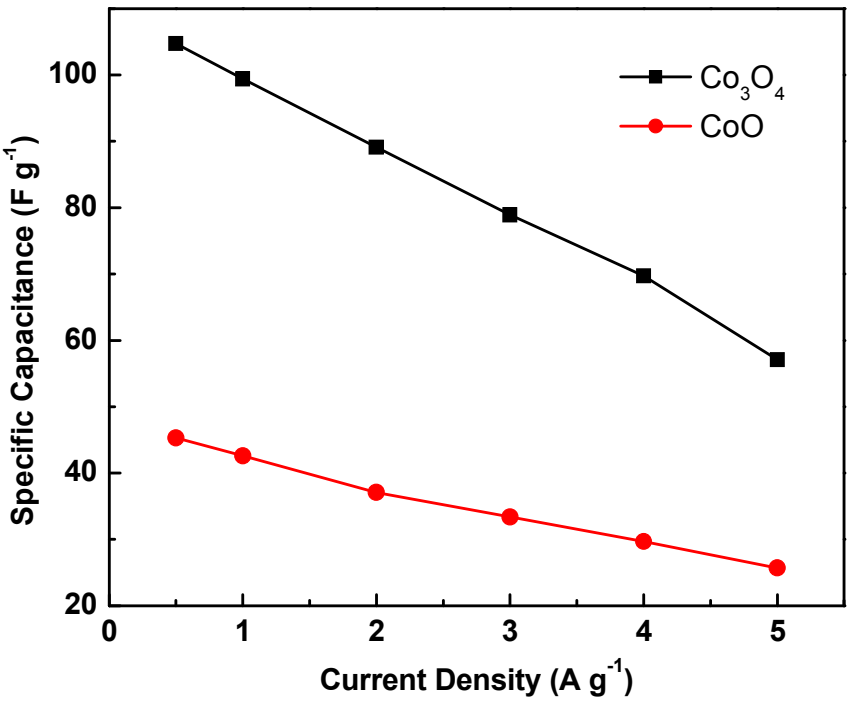

Figure 11

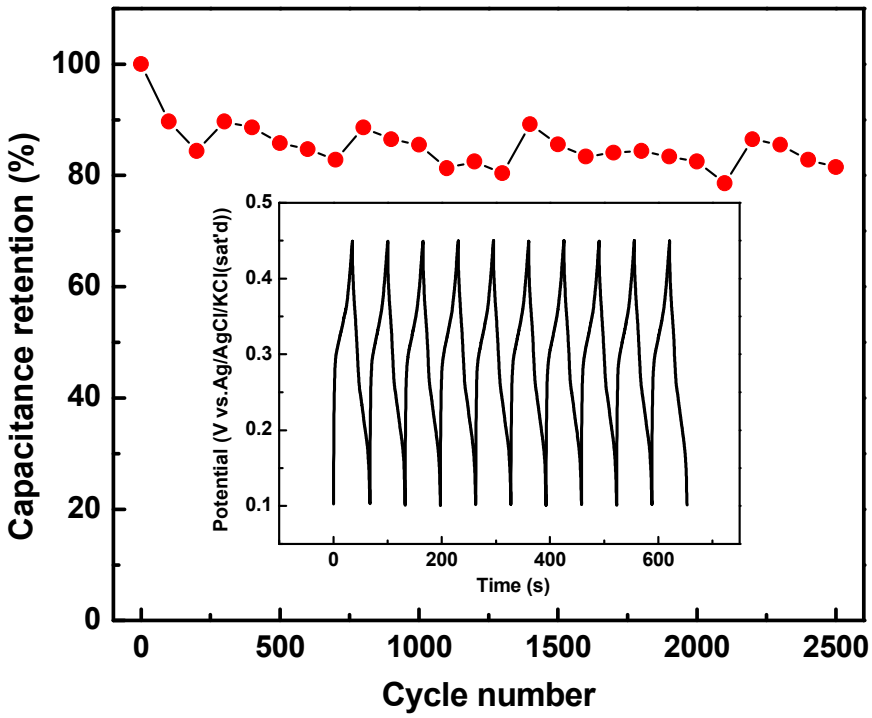

Figure 12

Synopsis

1D-3D Mixed-Ligand Frameworks with an Unusual *dmp* Topology Tuned by Intersection Angles of Isomeric Benzenedicarboxylates: Magnetic Properties, Gas-Dependent Calcination-thermolysis and Energy Storage Performances

Zuo-Xi Li,* Gan Ye, Juan Han, Ying Yang, Kang-Yu Zou, Xin Wang, Xiao-Ling Wang and Xiao-Feng Gou

Three coordination polymers were prepared to study the structural diversity, and corresponding magnetic properties have been well investigated. CoO and Co_3O_4 particles were obtained from the gas-controllable calcination-thermolysis, which can be applied as supercapacitors.